PCCP

Electronic Structure and Energetics of a Heterodimeric BChl g'/Chl a' Special Pair Generated by Exposure of Heliomicrobium modesticaldum to Dioxygen.

Journal:	*Physical Chemistry Chemical Physics*
Manuscript ID	CP-ART-08-2023-003915.R1
Article Type:	Paper
Date Submitted by the Author:	21-Sep-2023
Complete List of Authors:	Kaur, Divya; Brock University, Chemistry Ferlez, Bryan; Cornell University Landry, Patrick; Rensselaer Polytechnic Institute Biskup, Till; Physikalisch-Technische Bundesanstalt Abteilung 8 Medizinische Physik und metrologische Informationstechnologie Weber, Stefan; Albert-Ludwigs-Universitat Freiburg Golbeck, John; The Pennsylvania State University, Biochemistry and Molecular Biology Lakshmi, K.; Rensselaer Polytechnic Institute, Chemistry and Chemical Biology van der Est, Art; Brock University, Chemistry

ARTICLE

Electronic Structure and Energetics of a Heterodimeric BChl g'/Chl a' Special Pair Generated by Exposure of *Heliomicrobium modesticaldum* to Dioxygen.

Received 00th January 20xx,
Accepted 00th January 20xx

DOI: 10.1039/x0xx00000x

Divya Kaur[a,*], Bryan Ferlez[b,c], Patrick Landry[d], Till Biskup[e,f] Stefan Weber[e], John H. Golbeck[b,g*], K.V. Lakshmi[d,*] Art van der Est[a,*]

Heliobacteria are anoxygenic phototrophs that have a Type I homodimeric reaction center containing bacteriochlorophyll *g* (BChl *g*). Previous experimental studies have shown that in the presence of light and dioxygen, BChl *g* is converted into 8^1-OH-chlorophyll a_F (hereafter Chl a_F), with an accompanying loss of light-driven charge separation. These studies suggest that the reaction center only loses the ability to transfer electrons once both BChl *g'* molecules of the P_{800} special pair have been converted to Chl a_F'. The present work confirms that the partially converted BChl *g*'/Chl a_F' special pair remains functional in samples exposed to dioxygen by demonstrating its presence using hyperfine couplings obtained from Q-band ^{1}H ENDOR, 2D ^{14}N HYSCORE and DFT methods. The DFT calculations of the BChl *g'*/BChl *g'* homodimeric primary donor, which are based on the recently published X-ray crystal structure, predict that the unpaired electron spin is equally delocalized over both BChl *g'* molecules and provide an excellent match to the experimental hyperfine couplings of the anaerobic samples. Exposure to dioxygen leads to substantial changes in the hyperfine interactions, indicative of greater localization of the unpaired electron spin. The measured hyperfine couplings are reproduced in the DFT calculations by replacing one of the BChl *g'* molecules of the primary donor with a Chl a_F' molecule. The calculations reveal that the spin density becomes localized on BChl *g'* in the heterodimeric primary donor. Time-dependent DFT calculations demonstrate that conversion of either or both of the accessory BChl *g* molecules and/or one of the BChl *g'* molecules of P_{800} to Chl a_F' results in minor effects on the energy of the charge-separated states. In contrast, if both of the BChl *g'* molecules of P_{800} are converted a large increase in the energy of the charge-separated state occurs. This suggests that the reaction center remains functional when only one half of the dimer is converted, however, conversion of both halves of the P_{800} dimer leads to loss of function..

Introduction

Heliobacteria are anoxygenic phototrophic bacteria in the phylum *Bacillota* (formerly *Firmicutes*)[1] that live in soil and microbial mats under low levels of visible light and fix nitrogen but not carbon. To survive in these environments, they employ bacteriochlorophyll *g* (BChl *g*) pigments, which absorb near IR wavelengths. They have a Type I reaction center (RC) comprised of two pairs of protein subunits $(PshA/PshX)_2$ arranged with C_2 symmetry.[2] The heliobacterial reaction center (HbRC) is the simplest of the known RCs and is thought to be an evolutionary precursor of the highly evolved heterodimeric Photosystem I RC. There is significant interest in understanding how and why the RCs evolved from homodimeric to heterodimeric upon the advent of oxygenic photosynthesis. One possible approach to addressing this question is to selectively alter one half of a primitive homodimeric RC to study the effects on electron transfer function. However, this cannot be achieved by site-directed mutagenesis, as the PshA polypeptides of homodimeric RCs are encoded by a single gene. As an alternative approach, a recent study has suggested that it may be possible to introduce asymmetry in the chlorophyll pigments in the primary donor of HbRCs by controlled exposure to dioxygen.[3]

Fig. 1 shows the X-ray crystal structure of the electron transfer cofactors of the HbRC.[2] The special pair, P_{800}, is a BChl *g'* (the 13^2 epimer of BChl *g*) dimer located near the P (outer) side of the cytoplasmic membrane. Two branches of symmetric electron acceptors extend from P_{800} across the membrane toward the N (inner) side. Each branch consists of an accessory (Acc) BChl *g* and an 8^1-OH chlorophyll a_F (the subscript F refers to a farnesyl tail; hereafter Chl a_F) pair, referred to as the A_0 acceptor.[2] The two branches converge at the [4Fe-4S] cluster F_X on the cytoplasmic side of the membrane. Because the HbRC has exact C2 symmetry, the two branches of electron transfer

[a] Department of Chemistry, Brock University, St. Catharines, Ontario, L2S 3A1, Canada. Email: avde@brocku.ca & dmatta@brocku.ca
[b] Department of Biochemistry and Molecular Biology, The Pennsylvania State University, University Park, PA 16802, USA. Email: jhg5@psu.edu
[c] Present address: Department of Molecular Biology and Generics, Cornell University, Ithaca, NY 14853 USA
[d] Department of Chemistry and Chemical Biology and The '60 Baruch Center for Biochemical Solar Energy Research, Rensselaer Polytechnic Institute, Troy, NY 12180, USA E-mail: lakshk@rpi.edu
[e] Institut für Physikalische Chemie, Albert-Ludwigs-Universität Freiburg, 79104 Freiburg, Germany
[f] Present address: Physikalisch-Technische Bunesanstalt, Abbestraße 2-12, 10587 Berlin, Germany
[g] Department of Chemistry, The Pennsylvania State University, University Park, PA 16802 USA

cofactors are indistinguishable. This means it is not possible to probe their relative use, but the symmetry dictates that electron transfer is equally probably in each of them.

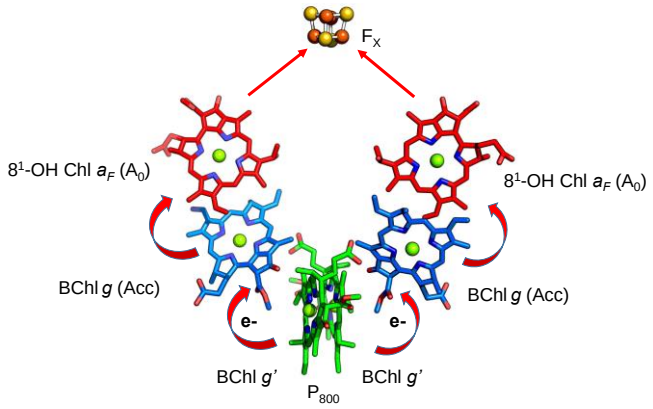

Fig. 1. Structure of the electron transfer cofactors of HbRC from the high resolution 2.2 Å resolution X-ray structure (PDB: 5V8K).[2] The electron transfer cofactors are denoted using the commonly accepted spectroscopic labels and the red arrows indicate the direction of electron transfer along the two branches. Shown in green, blue and red are the primary donor (P$_{800}$) BChl g'/BChl g', the accessory (Acc) BChl g and the acceptor (A$_0$) 8^1-OH Chl a_F, respectively The terminal acceptor [4Fe-4S] cluster F$_X$ is shown in yellow and orange

As illustrated in Fig. 2, in the presence of dioxygen BChl g[4,5] undergoes isomerization of the exocyclic double bond between the carbon atoms at position 8 and 8^1, with the addition of a hydroxyl group to carbon 8^1 resulting in its conversion to 8^1-OH-Chl a_F. In the HbRC, this leads to characteristic changes in the optical absorption spectrum and the loss of electron transfer activity. However, we have previously demonstrated that the loss of activity is non-linear as a function of percent conversion and complete loss of activity is observed only when all of the BChl g pigments have been converted to Chl a_F.[3] We were able to reproduce the shape of the activity versus conversion curve by assuming that (i) all BChl g pigments have an equal probability of being oxidized, (ii) the RC is inactive when both BChl g' molecules of the primary donor P$_{800}$ are oxidized, and (iii) the RC containing a partially converted primary donor with a BChl g'/Chl a_F' pair is active. This proposal was supported by the observation of altered back-reaction kinetics and changes in the transient electron paramagnetic resonance (EPR) spectra of partially oxidized samples[3] and changes in the photo-CIDNP NMR spectra.[6] However, the electronic properties of the proposed heterodimeric form of the primary donor, P$_{800}$, and the effect of pigment conversion on the energetics of electron transfer are yet to be studied in detail. Here, we use Q-dand ^{1}H electron nuclear double resonance (ENDOR), Q-band ^{14}N hyperfine sublevel correlation (HYSCORE) spectroscopy, and density functional theory (DFT) methods to probe the electronic structure of the primary donor radical cation P$_{800}^{\bullet+}$ in HbRC samples exposed to dioxygen. The energies of the charge-separated states are calculated using time-dependent DFT (TD-DFT) for RCs containing different combinations of BChl g and 8^1-OH-Chl a_F molecules in the primary donor P$_{800}$.

We find unequivocal support for the proposal of an active heterodimeric form of the primary donor P$_{800}$ in the partially oxidized HbRC.

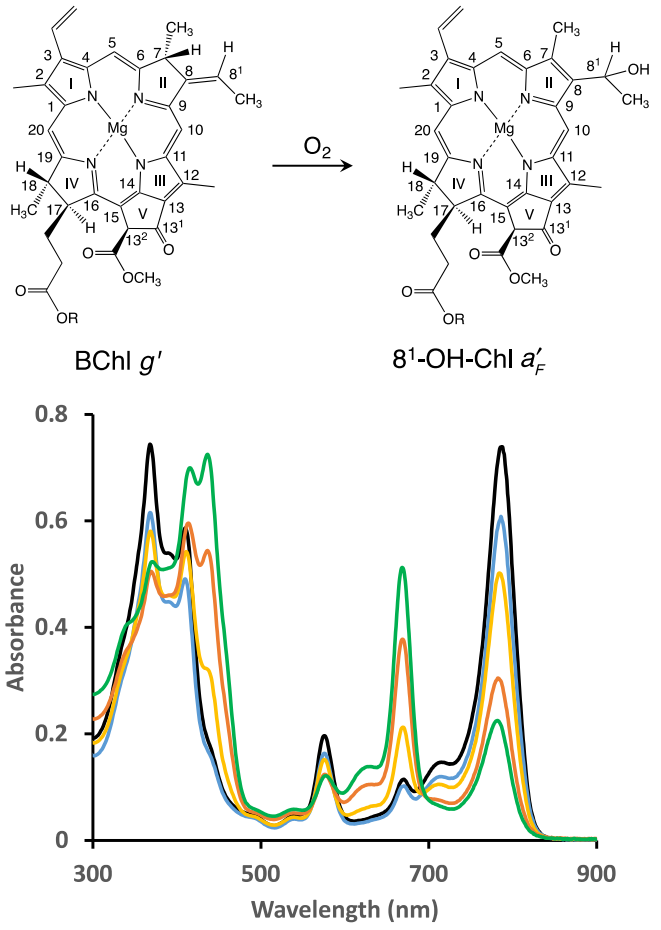

Fig. 2. Top: Isomerization of BChl g' to 8^1-OH-Chl a_F' (the subscript F refers to a farnesyl tail) in the presence of dioxygen. The numbering scheme for the atoms and pyrrole rings is in accordance with the IUPAC nomenclature.[7] Bottom: Optical absorbance spectra of HbRCs as BChl g' is converted to 8^1-OH-Chl a_F'. black: anaerobic, blue: 19% converted, yellow 34 % converted, orange 61% converted, green 72% converted.

2. Experimental Section

2.1 Growth and Isolation of HbRC

Preparation and purification of heliobacterial reaction centers (HbRC) were performed as previously described.[8] All manipulations were carried out under strict anaerobic conditions in dim green light. The final [BChl g] concentration of the HbRC sample was 2 mM BChl g in buffer containing 50 mM MOPS, pH 7.0, and 0.02% dodecyl maltoside. The sample was oxidized by first diluting anaerobic HbRCs 1.6-fold with oxic buffer (50 mM MOPS pH 7.0, and 0.02% dodecyl maltoside) at room temperature to a final concentration of 2 mM BChl g. The HbRCs were then exposed to atmospheric dioxygen in the dark while gently stirring until the amount of BChl g remaining was 28% of the amount present in the initial anaerobic sample (*i.e.* 72% BChl g was oxidized). The BChl g oxidation was monitored by periodically quantifying the decrease in intensity of the Qy absorption band of BChl g at 788 nm of 10 µl aliquots of the

HbRC solution after 40-fold dilution in buffer (50 mM MOPS pH 7.0, and 0.02% dodecyl maltoside). After the conversion of 72% of the BChl *g*, the samples were degassed with Ar for 15 min at 4 psi pressure and moved to an anaerobic chamber (98% N_2/2% H_2) where they were transferred to quartz EPR tubes and rapidly frozen at 77 K in the dark.

2.2 Pulsed Q-Band ENDOR and HYSCORE Spectroscopy

The ^{1}H ENDOR and ^{14}N HYSCORE experiments were performed using a Bruker Elexsys E580 pulsed EPR spectrometer equipped with a Bruker Q-FT EN 5107D2 Q-band-ENDOR resonator, Amplifier Research 250A250 RF amplifier and, a Tektronix TDS 684A oscilloscope. The temperature was controlled with an Oxford Instruments CF-935 cryostat and ITC 503 temperature controller.

The Davies ENDOR spectra were recorded at 25 K. The echo amplitude was measured at the maximum of the field-swept echo spectrum using the pulse sequence (π–*RF*–π/2–τ– π–echo). The π/2 microwave pulse length was 40 ns with a pulse spacing of τ = 200 ns defined as the difference in the starting point of the pulses. The delay between the second and third microwave pulses was 13 µs during which a 10 µs rf pulse was applied starting 1 µs after the first microwave pulse. Typically, 800 scans of the Davies ENDOR spectrum were collected.

Numerical simulation of the ^{1}H ENDOR spectra was performed using the "salt" function of the EasySpin software package version 5.2.35.[9,10] The ENDOR spectra of the groups of equivalent nuclei were calculated separately and summed to give the total spectrum. The intensities of the individual components were weighted by the number of equivalent nuclei and the Davies ENDOR intensity function:

$$V(\eta_s) = V_{max}\left(\frac{\sqrt{2}\eta_S}{\eta_S^2 + 1/2}\right)$$

where $\eta_S = A_{eff}\tau_\pi/2$ and A_{eff} is the effective hyperfine couplings and t_p is the length of the microwave p-pulse.[11] The calculated spectrum was fitted to the experimental spectrum using the "esfit" function of EasySpin by varying the hyperfine coupling constants and linewidths of each group of equivalent nuclei.

The 2D ^{14}N HYSCORE spectra were also acquired at 25 K. The echo amplitude was measured using the 4-pulse sequence (π/2–τ–π/2–t_1–π–t_2–π/2–τ–echo) [12] with a τ delay of 200 ns. The pulse lengths of the π/2- and π-pulses were 16 ns and 32 ns, respectively. The echo intensity was measured as a function of t_1 and t_2, where t_1 and t_2 were incremented in steps of 16 ns from an initial value of 300 ns. A total of 128 steps were used for each dimension. The unwanted echoes were eliminated by applying a 4-step phase cycling procedure. Typically, between 1 and 10 scans of the ^{14}N HYSCORE spectrum were collected with 10 averages for each value of τ. The signals were acquired at a magnetic field position corresponding to the peak of the field-sweep echo-detected EPR spectra in Fig. 3 to ensure maximum signal-to-noise and resolution of the HYSCORE spectra. To assign the four hyperfine coupled ^{14}N atoms to specific sites in $P_{800}^{\bullet+}$, we performed numerical simulations of the experimental Q-band ^{14}N HYSCORE spectra using the "saffron" function of the EasySpin software package, version 5.2.35,[9,10] to obtain their quadrupolar and hyperfine parameters for comparison with quantum chemical calculations. The observation of pronounced cross-peaks in the spectrum permits these parameters to be determined through numerical simulations of the experimental spectrum. Each set of cross-peaks in the spectrum is uniquely defined by the principal components of the hyperfine tensor, A_x, A_y and A_z, in combination with the quadrupolar coupling constant, *K*, and asymmetry parameter η. The parameter *K* describes the strength of the interaction between the nuclear quadrupole moment *Q* and the electric field gradient, *q*, and is given by: $K = e^2\,qQ/4\,\hbar$.[13,14] The asymmetry parameter describes the deviation of the quadrupole coupling tensor from axial symmetry. The simulations provide an accurate determination of hyperfine components and the value of $K^2(3+\eta^2)$. We obtained the best fit of the simulated and experimental spectra with the hyperfine parameters presented below in Table 3.

2.3 DFT Calculations

Geometry optimization of native $P_{800}^{\bullet+}$ The atomic coordinates for the native P_{800} with the axial His537 ligands were obtained from the X-ray crystal structure of the intact HbRC from wild-type *Heliobmicrobium* (formerly *Heliobacterium*) *modesticaldum* (PDB ID: 5V8K).[2] Geometry optimization was performed at the density functional level of theory (DFT) using the ORCA 5.0.1 package.[15] Two sets of calculations were performed for the geometry optimization. In the initial calculation, the long isoprenoid chains of the P_{800} chlorophylls were truncated to 4 carbon atoms terminating in a methyl group and optimization of the radical cation $P_{800}^{\bullet+}$ state was carried out without constraints. The axial histidine ligands were not included in this model and a CPCM solvent model with a dielectric constant (ε) of 4 was used to mimic the surrounding protein environment. The calculations were optimized with different combinations of functionals and basis sets, which included the B97-3c[16], B3LYP and PBE functionals[17] with the EPR-III basis set for the lighter elements and the 6-31G(d)[18,19] basis set for the central Mg^{2+} ion. The final calculations were carried out with the PBE functional and EPR-III basis set for lighter elements and 6-31G(d) for the Mg^{2+} ion. The atom-wise dispersion correction D3(BJ)[20,21] was also included in the calculations. The speed of the Coulomb integral calculations was enhanced using the resolution of identity (RI) approximation[22,23] in combination with Weigend's universal Def2/J auxiliary basis set.[24] The tighter convergence criteria (for both geometry and SCF) with default grid settings (defgrid2) were utilized in the calculation.

The initial $P_{800}^{\bullet+}$ model was further optimized by including the axial ligand His537 coordinated to the central Mg^{2+} ion of each (B)Chl molecule of the dimer. Geometry optimization was performed by constraining the His537 residues to a fixed conformation corresponding to the X-ray crystal structure and using a protocol similar to the naked dimer model described above.

Calculation of the EPR Parameters The geometry-optimized coordinates of the larger computational model including the axial ligands were used for single point calculations of hyperfine tensors of both protons and nitrogen-14 atoms of the dimeric

radical cation $P_{800}^{\bullet+}$. The calculations were done using the ORCA suite of programs (version 5.0.1)[15] with the same parameters, basis sets for atoms, and approximations described above for the geometry optimization calculation. A cube file of the electron spin density distribution was calculated from the ORCA output using the program orca_plot and visualized using the program VMD.

Geometry Optimization and Calculations of EPR Parameters for the Heterodimer BChl *g*'/Chl a_F' Radical Cation The initial model of the heterodimeric form of P_{800} was generated from the atomic coordinates of the X-ray crystal structure by converting one BChl *g'* molecule to 8^1-OH-Chl a_F' using the program Avogadro[25] to add an OH group at the 8^1 position and deleting the hydrogen atom at position 7 while keeping all other atoms the same. The geometry was then optimized and the EPR parameters were calculated using the same protocol as employed for $P_{800}^{\bullet+}$.

2.4 TD-DFT Calculations

The atomic coordinates of BChl *g'* 1001, the accessory BChl *g* 1002, His537, Gln 458 and H_2O 1276 for one half of the RC were obtained from the X-ray crystal structure of RCs from wild-type *H. modesticaldum* (PDB ID: 5V8K).[2] Missing hydrogen atoms were added to the structure, the backbone atoms of the amino acids were removed and replaced by a hydrogen atom and the isoprenoid side chains of the chlorophyll molecules were truncated to four atoms terminating in a methyl group. The coordinates of the second half of the RC were then generated by applying a 180° rotation about the symmetry axis to the coordinates of the first half, thus generating a symmetric dimer. DFT optimization of the model proved to be prohibitively expensive and therefore the geometry was optimized in Avogadro[25] using the UFF force field. To generate coordinates for the partially oxidized RCs, individual BChl *g* molecules were modified to Chl a_F using Avogadro and the structure was re-optimized.

TD-DFT calculations of the UFF optimized structures were performed in the ORCA 5.0.1 software package.[15] The ωB97X-D3 range-separated hybrid functional[26] was used with the def2-SVP basis set.[27] The RIJCOSX approximation[28] was used with the Def2-SVP/C and Def2/J auxiliary basis sets.[29,30] The Tamm-Dancoff approximation was not used in the TD-DFT part of the computations.

2.5 Modeling of RC activity

The populations of the specific pigment combinations were calculated as a function of total BChl *g* content by multiplying the fractional bulk pigment abundance of BChl *g* and Chl *a* for each position of a 4 (bacterio)chlorophyll model (i.e. two donor and two acceptor pigments). For example, the population of RCs with two oxidized accessory pigments (Chl *a*, Chl *a*) and a heterodimeric special pair (Chl *a*, BChl *g*) at the point when 30% of all BChl *g* is converted to Chl *a* (*i.e.* 70% BChl *g* remaining and 30% Chl *a* formed) is calculated by multiplying (0.3)Donor1 Chl *a**(0.7) Donor2 BChl *g* *(0.3)Acc.1 Chl *a**(0.3) Acc.2 Chl *a*, to give a fractional population of RCs with this arrangement of 0.0189. However, because in this case there two equivalent arrangements with a heterodimeric special pair (i.e. Donor2 could be oxidized instead of Donor1 as written in the example), this product is multiplied by two, resulting in 0.0378, or 3.78%. Using these percentages, the activity of the RC can be calculated for different possible assumptions for the activity of the specific pigment combinations.

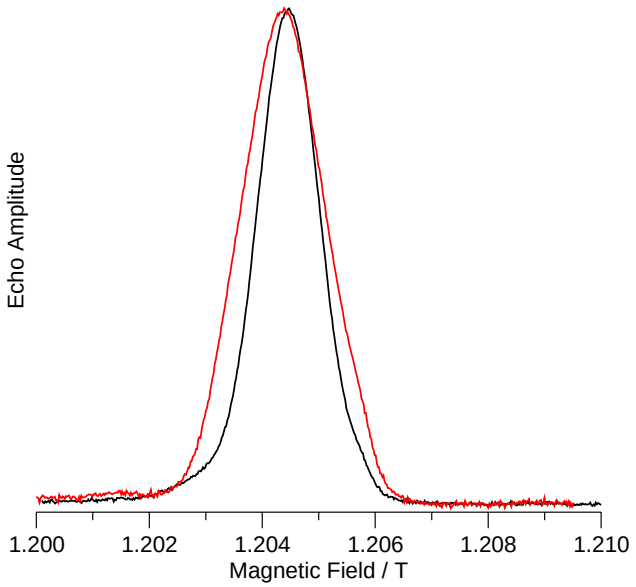

Fig. 3. Field-swept electron-spin echo Q-band spectra of $P_{800}^{\bullet+}$ in HbRCs at 25 K. The $P_{800}^{\bullet+}$ spectrum of the intact anaerobic HbRC is shown in black and the $P_{800}^{\bullet+}$ spectrum of the dioxygen exposed HbRC with 72% conversion of BChl *g* to Chl a_F by exposure to dioxygen in the dark is shown in red. The spectra are normalized to the same maximum amplitude and a microwave frequency of 33.759 GHz.

3. Results

3.1 Q-band field-swept echo-detected EPR spectroscopy

Fig. 3 shows the Q-band field-swept echo-detected EPR spectrum of the primary donor cation, $P_{800}^{\bullet+}$, of the HbRC measured under continuous illumination. The spectrum from an anaerobic HbRC sample is shown in black, while that of RCs exposed to dioxygen for 8 hours (referred to as the 'dioxygen-exposed' sample) is shown in red. Consistent with previously reported X-band transient EPR spectroscopy studies[3], there is distinct broadening of the $P_{800}^{\bullet+}$ EPR spectrum of the dioxygen-exposed HbRC sample. Because the line width of the spectrum is governed largely by unresolved hyperfine couplings, the broadening suggests that these couplings increase upon dioxygen exposure, possibly as a result of greater localization of the unpaired electron. In a previous study,[3] we proposed that if one of the BChl *g'* molecules of P_{800} was converted to Chl a_F', the asymmetry of the resulting heterodimer would lead to greater localization of the unpaired electron spin on one of the two chlorophyll molecules. In such a scenario, the line widths of the X- (9.6 GHz) and Q-band (35.5 GHz) spectra are predicted to increase by a factor of $\sqrt{2}$.[31] Consistent with this prediction, the line width of the previously reported X- and Q-band transient EPR spectra[3] increases from 0.435 mT in anaerobic samples to 0.60 mT upon dioxygen exposure, which is close to the expected factor of $\sqrt{2}$. However, the change in line width is not conclusive evidence for a change in the hyperfine couplings due to localization of the unpaired electron spin on one of the chlorophylls because there are other phenomena that may

contribute to line broadening in EPR spectra. Thus, direct experimental measurement of the hyperfine couplings by ENDOR and HYSCORE spectroscopy and quantitative predictions using quantum chemical calculations are needed to determine the extent the delocalization of the unpaired electron spin.

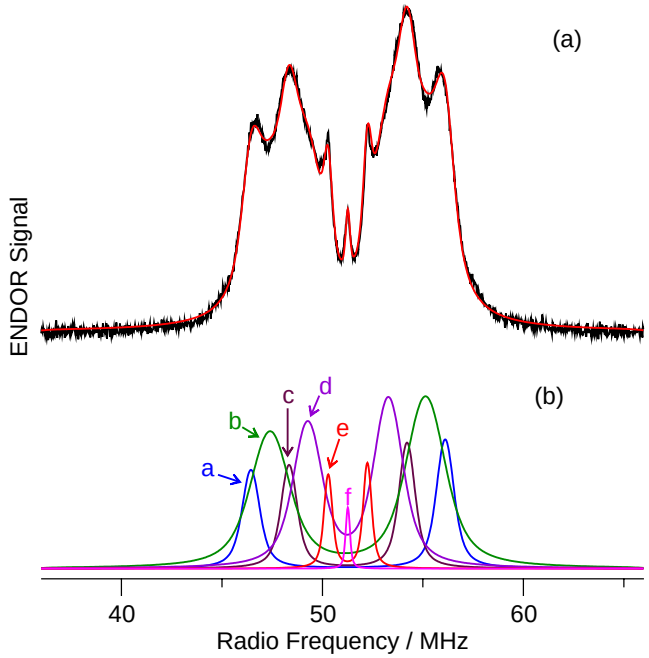

Fig. 4 Experimental and simulated Q-band ENDOR spectra of $P_{800}^{\bullet+}$ in intact anaerobic HbRCs. (a) Experimental (black) and simulated (red) spectra. (b) Spectral contributions of the individual hyperfine coupled protons or groups of equivalent protons to the simulated spectrum shown in part (a). The hyperfine couplings of components a-f are given in Table 1. Details of the simulation are provided in the text. Microwave frequency: 33.744 GHz, Magnetic field: 1.2039 T.

Table 1. Experimental and calculated isotropic hyperfine couplings of $P_{800}^{\bullet+}$ in intact anaerobic HbRCs. The uncertainty in the experimental A_{iso} values is ± 0.1 MHz. The sign of the A_{iso} couplings have been chosen by comparison with the DFT values calculated using the PBE functional with the EPR-III basis set for the C, H, N and O atoms and 6-31G(d) for the Mg atom. The label refers to the components shown in Fig. 4b.

Label	Assignment	This work	Ref [32]	Ref [33]	DFT
a	7 CH	9.7	9.3	-	7.8
b	8^1 CH_3	7.7	6.5	-	6.1
c	8^1 CH	–5.9	-	–5.0	–5.3
d	12 CH_3	4.0	3.6	3.7	4.4
e	2 CH_3, 17, 18 CH	1.9	2.0	1.8	2.1, 3.3, 2.0
f	all other protons	0	-	-	≤ 1.0

3.2 Q-band pulsed ^{1}H ENDOR spectroscopy

Shown in Fig. 4(a, b) are the experimental (black) and simulated (red) Q-band ^{1}H ENDOR spectrum of $P_{800}^{\bullet+}$ of intact anaerobic HbRC and the simulated contributions of individual hyperfine coupled protons, respectively. The anisotropy of the hyperfine couplings is not resolved in the spectrum and each coupling has been modeled by a single isotropic coupling (A_{iso}) value. The spectrum can be reproduced using two CH protons and two CH_3 groups with moderately strong couplings (> 3 MHz). The weak coupling at ~ 2 MHz has been modeled as a single proton. However, because of the suppression of weak couplings by the Davies ENDOR pulse sequence the number of protons may be underestimated. A feature at the proton Larmor frequency is also included.

Table 1 presents the proton hyperfine coupling constants obtained from the numerical fit of the spectrum along with previously reported values[32,33] and the predicted couplings obtained from the DFT calculations. Using the calculated proton hyperfine coupling values obtained by DFT as a guide, we assign the two largest CH couplings to the protons at the C-7 and C-8^1 positions and the two largest CH_3 couplings to the methyl groups at the C-8^1 and C-12 positions of BChl *g* (see Fig. 2 for the numbering scheme). The coupling at ~2 MHz is assigned to a combination of the C-2 methyl protons and the β protons at C-17 and C-18. The calculations show that the hyperfine couplings of the C-8^1 methyl protons is larger than those of the C-12 methyl group, which is in contrast to the assignment in the literature.[32] They also reveal that the C-7 CH proton is the only one of the β-protons with a large coupling. The DFT calculations show that the couplings to all other protons are small and contribute to the matrix line at the center of the ENDOR spectrum. By comparing different basis sets and different possible models for the surrounding protein, we estimate the uncertainty in the DFT values to be approximately ±1.5 MHz. With the exception of the C-7 β-proton all of the experimental couplings are well within these error limits

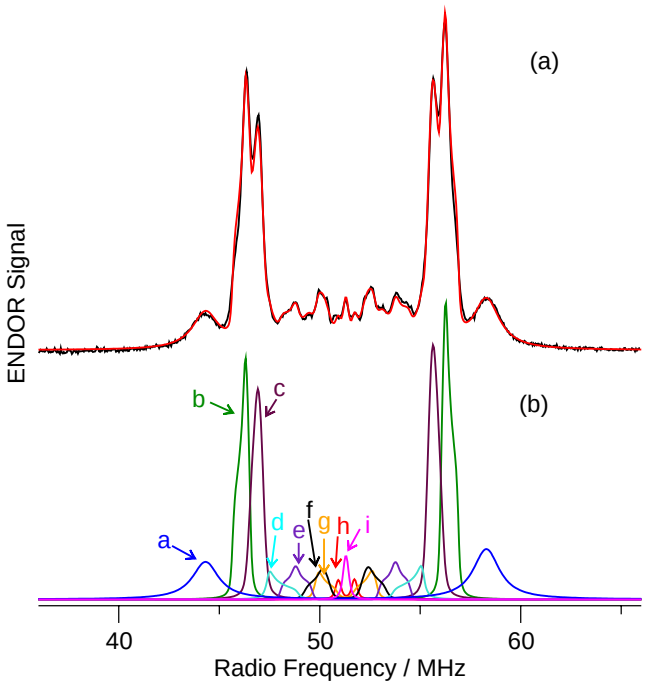

Fig. 5 (a) Experimental (black) and simulated (red) Q-band ^{1}H ENDOR spectrum of $P_{800}^{\bullet+}$ in dioxygen exposed HbRCs. (b) Contributions of individual hyperfine coupled protons or groups of equivalent protons to the simulated spectrum of $P_{800}^{\bullet+}$ in dioxygen exposed HbRCs. The hyperfine couplings of components a-i are given in Table 2. Details of the simulations are provided in the text. Microwave frequency 33.775 GHz, Magnetic field: 1.2052 T.

Fig. 5 shows the corresponding Q-band pulsed ^{1}H ENDOR spectrum of $P_{800}^{\bullet+}$ in HbRCs exposed to dioxygen, in which 72% of the BChl *g* has been converted to Chl a_F. As is immediately

apparent, the ^{1}H ENDOR spectrum of $P_{800}^{\bullet+}$ is different from that of the anaerobic sample (Fig. 4 (a)). The most obvious difference is the presence of the peaks on the outer edges of the spectrum that correspond to a proton hyperfine coupling that is significantly larger than the largest coupling in the anaerobic sample. This implies that the unpaired electron is more localized and clearly supports the idea of an altered form of P_{800} in the dioxygen-exposed sample. Initial attempts to fit the spectrum using isotropic hyperfine couplings did not give acceptable agreement. We postulated that this was because the increase in the hyperfine couplings that is apparent in the spectrum also leads to partial resolution of the anisotropy of the hyperfine tensors. Therefore, the three principal values of each hyperfine tensor were included. The choice of starting values of the hyperfine components for the fit was guided by DFT calculations in which one of the two BChl *g'* molecules of P_{800} was converted to Chl a_F'. The fitted hyperfine couplings and the corresponding DFT values are presented in Table 2. An important consideration in assigning the proton hyperfine couplings is the fact that the dioxygen-exposed sample contains a mixture of the three possible different forms of P_{800}: BChl *g'*/ BChl *g'*, BChl *g'*/Chl a_F', and Chl a_F'/Chl a_F'. Complete conversion of BChl *g* to Chl a_F renders the RC inactive, thus the Chl a_F' homodimer should not contribute to the $P_{800}^{\bullet+}$ ENDOR spectrum. Based on the analysis of the activity as a function of percent BChl *g* conversion curve reported in Ferlez et al.[3], we estimate that when 72% of the BChl *g* is converted, 84% of the active P_{800} is the heterodimeric BChl *g'*/Chl a_F' form and the remaining 16% is the BChl *g'*/BChl *g'* form. Thus, we assign all of the stronger ENDOR peaks corresponding to couplings larger than 4 MHz to the heterodimer, while the assignment of the weaker couplings is uncertain. As can be seen in Table 2, there is good agreement between the measured hyperfine couplings and those obtained from the DFT calculations using a heterodimeric BChl *g'*/Chl a_F' model.

Table 2. Experimental and calculated isotropic hyperfine couplings, A_{iso}, of $P_{800}^{\bullet+}$ in dioxygen exposed HbRCs. The experimental values were obtained from the numerical simulations shown in Fig. 5. The labels refer to the components shown in Fig. 5b. The uncertainty in the ENDOR values is ± 0.1 MHz.

Label	Assignment		A_{xx} / MHz	A_{yy}/ MHz	A_{zz} / MHz	A_{iso} / MHz
a	7 CH	ENDOR	14.0	14.0	14.0	14.0
		DFT	14.15	15.27	16.48	15.30
b	8^1 CH_3	ENDOR	9.5	10.0	11.2	10.2
		DFT	11.81	12.22	14.37	12.80
c	12 CH_3	ENDOR	8.1	8.7	9.6	8.8
		DFT	7.61	7.99	9.85	8.48
d	17 CH	ENDOR	4.7	7.6	7.8	6.7
		DFT	5.26	5.81	7.43	6.17
e	18 CH	ENDOR	3.3	5.0	6.5	5.0
		DFT	4.04	4.52	5.92	4.83
f	-	ENDOR	1.5	2.3	4.1	2.6
g	-	ENDOR	0.8	2.9	2.9	2.2
h	-	ENDOR	0.8	0.8	0.8	0.8
i	matrix		0	0	0	0

3.3 Q-band ^{14}N HYSCORE Spectroscopy

Shown in Fig. 6 (a, b) are the experimental (blue) and simulated (pink) Q-band ^{14}N HYSCORE spectra of $P_{800}^{\bullet+}$ under intact anaerobic and dioxygen exposed conditions, respectively. The cross-peaks in both the experimental and simulated ^{14}N spectrum arise from the electron-nuclear hyperfine interactions of the unpaired electron spin (S = ½) with the nuclear spin (I = 1) of the nitrogen (^{14}N) atoms of $P_{800}^{\bullet+}$.

Intact anaerobic HbRCs The spectrum in Fig. 6 (a) displays cross-peaks from four types of ^{14}N atoms that are hyperfine-coupled to the unpaired electron spin of $P_{800}^{\bullet+}$ in intact anaerobic HbRCs. Typically, the spectral features arising from ^{14}N atoms that are weakly to moderately hyperfine coupled to the unpaired electron spin (when $A < 2\nu_N$, where ν_N is the Larmor frequency of the ^{14}N nucleus) lead to cross-peaks in the (+,+) quadrant, while any strong hyperfine couplings (when $A > 2\nu_N$) manifest as cross-peaks in the (-,+) quadrant of a HYSCORE spectrum.[12–14]

The four distinct pairs of cross-peaks observed in the (+,+) quadrant of the spectrum in Fig. 6 (a) are symmetric about the diagonal. These cross-peaks are assigned to the weakly hyperfine coupled ^{14}N atoms interacting with the unpaired electron spin of $P_{800}^{\bullet+}$. The first well-pronounced, intense cross peak in the (+,+) quadrant is located at a frequency ~2.7 MHz, which is close to the ^{14}N Zeeman frequency (~ 3.69 MHz and is assigned to the single quantum (SQ) transition of a weakly hyperfine coupled ($A < 2\nu_N$) ^{14}N atom. Additionally, there are three pairs of cross peaks of much weaker intensity that are also symmetric with respect to the diagonal. These are assigned to the single- and double-quantum transitions of three weakly coupled ^{14}N atoms. The separation of all of the peaks along the diagonal is due to hyperfine interactions of the nucleus with the unpaired electron spin of $P_{800}^{\bullet+}$.

Fig. 6 Experimental (blue) and simulated (pink) Q-band 2D ^{14}N HYSCORE spectra of $P_{800}^{\bullet+}$ in (a) intact anaerobic and (b) dioxygen-exposed HbRCs. Microwave frequency 33.775 GHz, Magnetic field: 1.2052 T.

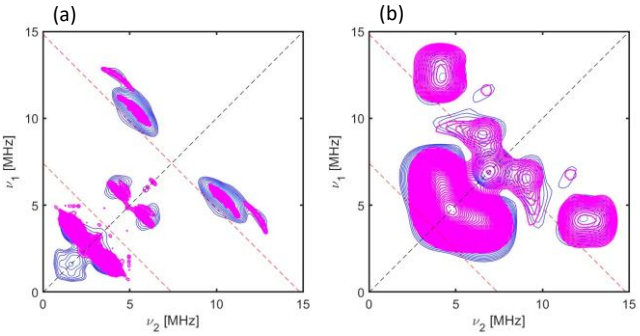

As shown in Table 3, the values of the quadrupolar coupling constants obtained from the numerical simulations (see Methods section) are ~0.7 MHz for the four hyperfine coupled ^{14}N atoms. The coupling constants obtained from the simulations are similar to those reported for other related systems. [34–38] This is consistent with the assignment of the couplings to the four pairs of symmetry related nitrogen atoms of the two BChl *g'* molecules of $P_{800}^{\bullet+}$. Also shown in Table 3 are ^{14}N hyperfine couplings obtained from DFT calculations of

$P_{800}^{\bullet+}$ and [BChl *g'*]$^{\bullet+}$. The experimental and calculated couplings of $P_{800}^{\bullet+}$ are in good agreement, which allows the experimental couplings to be assigned to specific ^{14}N atoms labeled I – IV in reference to the four pyrrole rings as shown in Fig. 2. As can be seen in Table 3, the $P_{800}^{\bullet+}$ hyperfine couplings are roughly a factor of two smaller than those of monomeric [BChl *g'*]$^{\bullet+}$ indicating that the spin density is symmetrically delocalized over the two BChl *g'* rings in $P_{800}^{\bullet+}$. The sign of the hyperfine couplings cannot be obtained from HYSCORE data, but negative experimental values are reported in Table 3 based on the signs obtained from the DFT calculations.

Table 3. Experimental and calculated isotropic ^{14}N hyperfine couplings in MHz of $P_{800}^{\bullet+}$ in intact anaerobic HbRCs. The experimental hyperfine couplings were determined by spectral simulations of the Q-band 2D ^{14}N HYSCORE spectrum shown in Fig. 6 (a). The respective signs and assignments of the experimental couplings were deduced by comparison with the computed couplings, which were obtained from DFT computations using the PBE functional and the EPRIII / 6-31G(d) basis set.

Nitrogen	Experiment A_{iso} / MHz	DFT $P_{800}^{\bullet+}$ A_{iso} / MHz	DFT [BChl g'] $^{\bullet+}$ A_{iso} / MHz
N^{I}	–1.0 ± 0.1	–0.82	–1.56
N^{II}	–1.5 ± 0.1	–1.23	–2.48
N^{III}	–0.9 ± 0.1	–0.80	–1.69
N^{IV}	–1.2 ± 0.1	–0.98	–2.12

Dioxygen Exposed HbRCs The 2D ^{14}N HYSCORE spectrum of dioxygen exposed HbRCs shown in Fig. 6 (b) displays cross-peaks that arise from multiple ^{14}N atoms that are hyperfine-coupled to the unpaired electron spin of the donor radical cation. Once again, the presence of cross-peaks in the (+,+) quadrant in Fig. 6b suggests that the spectral features are due to ^{14}N atoms which are weakly to moderately hyperfine-coupled to the unpaired electron spin (when $A < 2\nu_N$).**[12]** Based on the ENDOR results and the dependence of the activity of the RCs versus the percent conversion, we expect that the cross-peaks arise primarily from the (BChl *g'*/Chl a_F')$^{\bullet+}$ heterodimeric form of the donor with a possible weak contribution from intact $P_{800}^{\bullet+}$.

Given the broadening in this spectrum, which likely arises from the heterogeneity of the sample, the hyperfine parameters calculated using DFT methods were used as a starting point to guide the ^{14}N HYSCORE simulations. To adequately match the spectral features observed in the experimental spectrum without introducing unnecessary parameters, we used the eight hyperfine coupled ^{14}N atoms that are expected for a chlorophyll heterodimer.

The value of the quadrupolar coupling constant, K, was determined to be ~0.7 MHz for the hyperfine-coupled 14N atoms in keeping with their assignment to the nitrogen atoms in the (B)Chl ring(s).[34–36] The values of isotropic hyperfine couplings, Aiso, obtained from the fit are shown in Table 4 along with the corresponding values obtained from the DFT calculations. The fit to the experimental spectrum yields four larger couplings of magnitudes between 1.6 and 2.4 MHz and four smaller couplings ≤ 0.2 MHz, the values of which are not easily determined. The values of the four larger couplings are greater than those observed for the anaerobic sample (Table 3) and are similar to the calculated values for [BChl g']•+ suggesting that the unpaired electron spin is predominantly localized on one of the (B)Chl molecules in the heterodimer. This is borne out by the DFT calculations of the heterodimer, which show that spin density is localized to a large extent on the BChl g' half of the heterodimer (Fig. 7). Based on the comparison between the experiment and couplings, we assign the former values to specific nitrogen atoms and adopt the predicted sign. The assignments are not certain for the four small couplings arising from the Chl aF' half of the dimer.

Table 4. Experimental and calculated isotropic ^{14}N isotropic hyperfine couplings, A_{iso}, from dioxygen exposed HbRCs. The experimental hyperfine couplings were determined by spectral simulations of the Q-band ^{14}N HYSCORE spectrum in Fig. 6b. The signs of the experimental couplings and their assignment to specific nitrogen atoms is based on the computed couplings, which were obtained using the PBE functional and the EPRIII and 6-31G(d) basis set. The superscripts I-IV refer to the pyrrole ring as shown in Fig. 2. The subscripts *g* or *a* refer to BChl *g'* and Chl a_F' respectively.

Nitrogen	Experiment A_{iso} / MHz	DFT $P_{800}^{\bullet+}$ A_{iso} / MHz
N_g^{I}	–1.6±0.1	–1.40
N_g^{II}	–2.5±0.1	–2.04
N_g^{III}	–1.8±0.1	–1.45
N_g^{IV}	–2.0±0.1	–1.68
N_a^{I}	0.2±0.1	0.73
N_a^{II}	0.04±0.1	–0.20
N_a^{III}	0.02±0.1	0.20
N_a^{IV}	0.1±0.1	0.52

The difference between the isotropic ^{14}N hyperfine couplings obtained from the anaerobic and dioxygen-exposed HbRCs is consistent with those of the primary donor cations of homodimeric and heterodimeric RCs.[39] Previous ^{14}N HYSCORE and DFT studies of the $P_{840}^{\bullet+}$ donor in the homodimeric RCs of *C. thermophilum* and *Chlorobium limicola* showed four ^{14}N couplings of ~1 MHz. [38,40] In contrast, for $P_{700}^{\bullet+}$ and $P_{865}^{\bullet+}$ in heterodimeric Photosystem I and RCs of purple bacteria two sets of hyperfine couplings were observed at ~2 MHz and 0.5 MHz, respectively.[41,42] For anaerobic HbRCs, the electron spin density is distributed equally over the two BChl *g'* molecules and the hyperfine couplings are similar to those of the primary donor radical cation of other homodimeric RCs. In contrast, in the dioxygen-exposed sample the spin density is localized on the BChl *g'* half of the heterodimer and the hyperfine couplings are similar to the calculated values of monomeric [BChl *g'*]$^{\bullet+}$ radical cation (Table 3) and are comparable to those of $P_{700}^{\bullet+}$ in PS I.[39,43–45] In the latter, the ratio of electron spin density across the Chl *a*/Chl *a'* dimer is 5:1 or 6:1 in favor of Chl *a* on the B-branch side of the RC.

3.3 Spin Density Calculations

We performed DFT calculations to further understand the electronic structure of the homodimeric BChl g and heterodimeric (BChl g'/Chl aF') P800•+ of the intact anaerobic and dioxygen exposed HbRC, respectively (Fig. 7 (a, b)). The initial computational models contained only the BChl g'/BChl g' and BChl g'/Chl aF' molecules as described above in the Experimental section. These models were then extended to include protein-cofactor interactions by adding the histidine

residues that are directly coordinated to the central Mg^{2+} ion of the chlorophyll molecules.

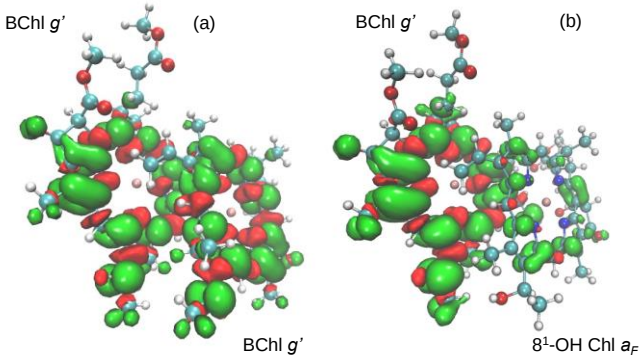

Fig. 7 Spin density distribution of (a) homodimeric (BChl *g'*/BChl *g*) and (b) heterodimeric (BChl *g'*/Chl *a'*) primary donor cation radical P_{800}^{+}. The positive and negative electron spin densities are rendered in green and red, respectively

Our results demonstrate that the electron spin density is uniformly distributed across both of the BChl *g'* molecules in the intact anaerobic homodimeric HbRC (Fig. 7a). However, in the dioxygen exposed heterodimeric state, the electron spin density is asymmetrically distributed with higher density on BChl *g'* than on Chl a_F' (Fig. 7b). As discussed above, the respective models reproduce the experimental hyperfine couplings observed in the ^{1}H ENDOR and 2D ^{14}N HYSCORE experiments (Tables 3 and 4).

3.4 TD-DFT calculations

Time-dependent density functional theory (TD-DFT) calculations can be applied to study the charge-separated states of the HbRC.[46,47] Such calculations provide vertical excitation energies but does not take the reorganization energy into account. They are also computationally expensive and can only be performed on somewhat restricted models of the RC. Despite these shortcomings, TD-DFT calculations provide a qualitative picture of the relative energies of possible charge-separated states and the localization of the electron and hole. This makes such calculations ideal for investigating the effect of the BChl *g* to Chl a_F conversion on the energetics of charge separation. Therefore we carried out TD-DFT calculations on a four-chlorophyll model[46] consisting of the P_{800} dimer and the two accessory chlorophylls to compare possible combinations of the BChl *g* and Chl a_F pigments in the four sites. The model also includes the axial histidine ligands to P_{800} (His537), the water molecule coordinated to the accessory BChl *g*, and Gln458 residue H-bonded to the water molecule. In preparing the atomic coordinates of the model, we found that the energy of the charge-separated states depends on the position of the hydrogen atom in the H-bond between Gln458 and the water molecule coordinated to the accessory chlorophyll. We have chosen to use a structure in which a proton is transferred from water to Gln458 because it lowers the energy of the charge-separated states by an amount that is comparable to that expected for the reorganization energy. Importantly, however, we do not draw any quantitative conclusions from the computations, meaning that this choice is not critical. The details of the procedures used for the TD-DFT computations are described in the Experimental section.

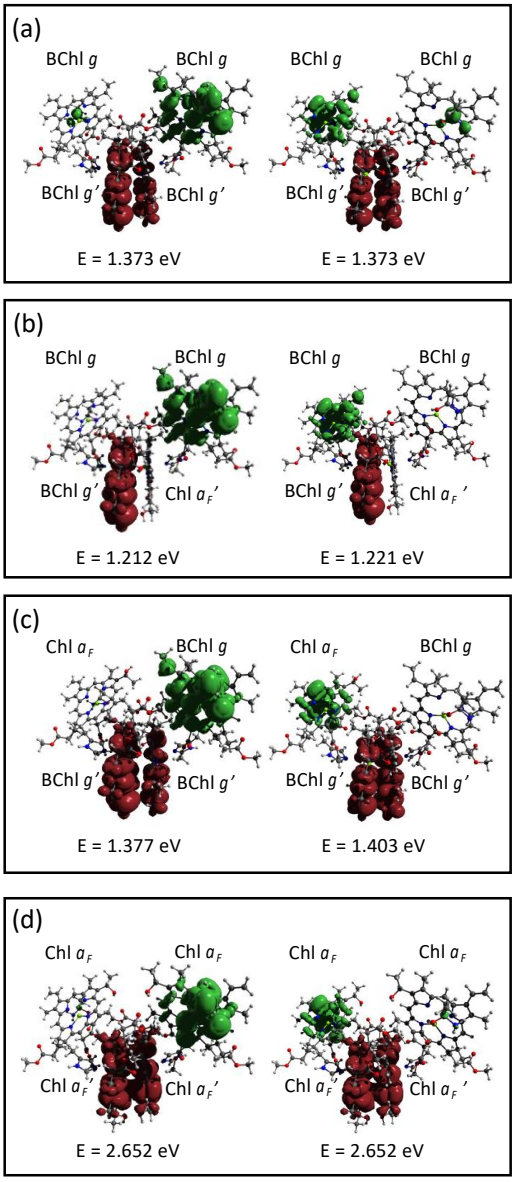

Fig. 8 TD-DFT electron density difference surfaces and energy of the charge-separated states in HbRCs with different chlorophyll compositions. (a): intact anaerobic HbRCs; (b) conversion of one BChl *g'* of P_{800} to Chl a_F'; (c) conversion of one of the accessory BChl *g* cofactors to Chl a_F (d) conversion of all BChl *g* and BChl *g'* cofactors to Chl a_F and Chl a_F'. Electron density loss is plotted in red and indicates the location of the hole in the charge-separated state. Electron density gain is plotted in green and shows the location of the transferred electron. The surfaces were plotted in Avogadro [25] with an iso value of 0.0001 and rendered using POV-Ray.

Shown in Fig. 8 are the density difference surfaces and corresponding energy of the lowest of the charge separated states. The red surfaces represent a loss of electron density between the ground state and charge-separated state and show the distribution of the electron hole produced by the charge separation. The green surfaces are positive density difference and represent the transferred electron. The intact HbRC is shown in Fig. 8a and as can be seen, two states with identical energy corresponding to electron transfer in the two branches

are obtained. As expected for a homodimer, and consistent with the ^{1}H ENDOR and ^{14}N HYSCORE data, the electron hole is distributed evenly over the two BChl *g′* of the donor. In Fig. 8b the chlorophyll on the right side of the P_{800} dimer has been converted to Chl a_F′. In agreement with the spin density calculations, this leads to localization of the electron hole on the BChl *g′* half of the dimer. The energy of the two charge separated states is now slightly different and the state in which the acceptor is in the same branch as BChl *g′* is lower in energy. Note that in the perspective shown in Fig. 8 the electron and hole appear on opposite sides of the complex when they are in the same branch. Both charge-separated states are slightly lower in energy than in the intact RC (Fig. 8a). In Fig. 8c one of the accessory chlorophylls has been converted to Chl a_F and the donor is the native BChl *g′* dimer. Again, this leads to a difference in energy between the two charge separated states and the state in which the electron is transferred to Chl a_F is predicted to be 26 meV higher in energy. In Fig. 8d all of the chlorophylls have been converted to Chl a_F. This results in a dramatic increase of 1.3 eV in the predicted energies of the charge separated states compared to the intact RC. The energies of the charge separated states in RCs with other combinations of BChl *g* (BChl *g′*) and Chl a_F (Chl a_F′) are shown in Table 5.

Table 5. Calculated energies of the charge separated states in a four-chlorophyll model of HbRCs with different possible arrangements of BChl *g,* BChl *g′,* Chl a_F and Chl a_F′. The energies have been obtained from TDDFT calculations.

Chlorophyll Arrangement	Charge Separated State	Energy (eV)
gg'g'g	[(BChl *g′*) $_2$] $^+$[BChl *g*]$^-$	1.373
ag'g'g	[(BChl *g′*) $_2$] $^+$[BChl *g*]$^-$	1.377
	[(BChl *g′*) $_2$] $^+$[Chl a_F]$^-$	1.403
ga'g'g	[BChl *g′*/Chl a_F′] $^+$[BChl *g*]$^-$	1.212, 1.221
aa'g'g	[BChl *g′*/Chl a_F′] $^+$[BChl *g*]$^-$	1.213
	[BChl *g′*/Chl a_F′] $^+$[Chl a_F]$^-$	1.250
aa'g'a	[BChl *g′*/Chl a_F′] $^+$[Chl a_F]$^-$	1.175, 1.187
ga'a'g	[(Chl a_F′) $_2$] $^+$[BChl *g*]$^-$	2.692
aa'a'a	[(Chl a_F′) $_2$] $^+$[Chl a_F]$^-$	2.652

Overall, we can draw the following main conclusions from the TDDFT calculations: i) The electron hole is delocalized evenly over the two BChl *g′* of P_{800} in intact HbRCs; ii) conversion of one of the BChl *g′* of P_{800} leads to localization of the electron hole on the BChl *g′* half of the heterodimer and a slight stabilization of the charge separated state energies; iii) conversion of either or both of the accessory chlorophylls has only a minor destabilizing effect on the charge separated state energies; and iv) conversion of both BChl *g′* of P_{800} results in a large increase in the charge separated state energies. All of these results indicate that the reduction midpoint potentials of BChl *g* and Chl a_F are similar but that the oxidation potential of Chl a_F′ is much higher than that of BChl *g′*. As a result, conversion of the acceptor chlorophylls should not greatly affect function but conversion of both of the BChl *g′* of P_{800} can be expected to make electron transfer energetically unfavorable.

4. Discussion

The ENDOR and HYSCORE data both show that the electron spin density distribution in the primary donor radical cation $P_{800}^{\bullet+}$ changes on exposure of HbRCs to dioxygen. In intact anaerobic HbRC samples, the electron spin density is distributed equally over the two BChl *g′* molecules of $P_{800}^{\bullet+}$, while in the dioxygen exposed sample, there is an increase in the measured hyperfine couplings indicating that unpaired electron spin density is more localized. The DFT and TD-DFT calculations show that it is the BChl *g′* half of the heterodimer that carries the unpaired electron and its associated spin density. The TD-DFT calculations of the four-chlorophyll model of the RC suggest that the loss of function that accompanies conversion of the chlorophylls is a result of a higher oxidation potential of Chl a_F compared to BChl *g*. This also explains why the spin density becomes localized on the BChl *g′* half of the heterodimer. The results indicate that electron transfer probably becomes energetically unfeasible when both BChl *g′* molecules of the donor have been converted but that conversion of the accessory chlorophylls does not have a substantial effect on their ability to function as electron acceptors. It is important to note that this model does not include the A_0 chlorophylls, and recent experimental and theoretical studies suggest that the initial charge separation may occur between the accessory BChl *g* and A_0[47–50]. Hence, we need to consider whether or not our findings are consistent with this model. If we assume that conversion of any of the BChl *g* or BChl *g′* molecules in the electron transfer chain prevents it from acting as an electron donor as suggested by the TD-DFT calculations, the question is then which of the of the BChl *g* or BChl *g′* molecules must act as an electron donor if long-lived charge separation is to occur. If the initial charge separation takes place between the accessory BChl *g* and A_0 it would have to be stabilized by hole transfer to P_{800}, which would only become energetically unfeasible when both of the BChl *g′* of P_{800} were converted. Function would be lost when both accessory chlorophylls *or* both BChl *g′* of P_{800} were converted. In contrast, if the initial charge separation were between P_{800} and the accessory BChl *g*, then conversion of the accessory chlorophylls probably would not lead to loss of function. However, it is also possible that the site of initial charge separation is different in intact anaerobic RCs and oxygen exposed RCs in which the accessory BChl *g* has been converted to Chl a_F. Thus, the initial charge separation might be between the accessory BChl *g* and A_0 in intact RCs but between P_{800} and the accessory Chl a_F in oxygen exposed RCs.

We have considered several possible scenarios and plotted the predicted activity versus percent conversion of BChl *g* to determine which of the possible models can be distinguished from one another. As shown in Fig. 9 we obtain three distinctly different activity curves. The orange curve is obtained if we assume that activity is lost if both chlorophylls of P_{800} are converted or both of the accessory BChl *g* are converted. The black curve is obtained if we assume that activity is lost only when both BChl *g′* of P_{800} are converted and the gray curve all when four chlorophyll molecules must be converted to abolish activity. The red and green circles are the experimental activity

measured by steady state flavodoxin reduction and P_{800} photobleaching, respectively, as reported in Ferlez et al..[3] As can be seen, the black curve agrees best with the experimental activity curve and the models in which the conversion of the accessory chlorophyll abolishes the activity (gray and orange curves) do not describe the data well. It should be noted that the implied, but unstated, premise of the curves in Figs. 4A and 4B of Ferlez et al.[3] was that the conversion of BChl *g* to Chl a_F in the accessory site would not affect charge separation. The present experimental and theoretical study supports this assumption. However, because the site of the initial charge separation could be different in intact and partially converted RC's we cannot distinguish between the two possible mechanisms of the initial charge separation.

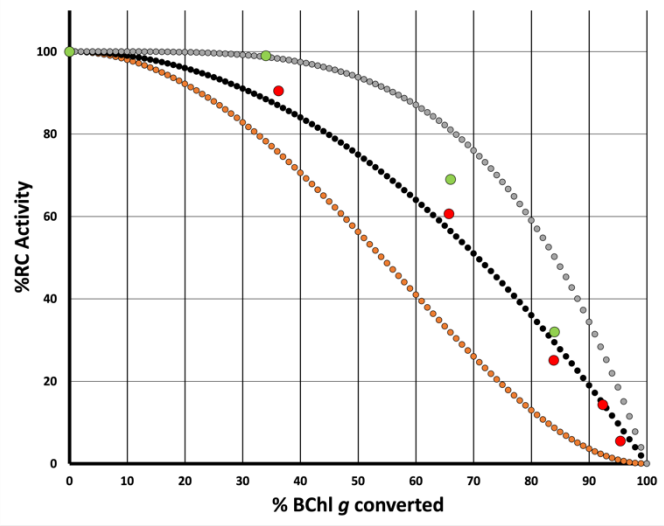

Fig. 9 Experimental activity[3] versus percent BChl *g* conversion compared to different possible models. Red circles: steady state flavodoxin reduction rate. Green circles: light induced P_{800} photobleaching. Orange: model in which activity requires at least one BChl *g* in P_{800} *and* in the accessory sites. Black: model in which activity requires at least one BChl *g* in P_{800}. Gray: model in which activity requires at least one BChl *g* in *either* P_{800} *or* the accessory sites.

Studies on photoaccumulated A_0^- could be useful in this regard. HYSCORE measurements of A_0^- in Photosystem I show that the acceptors Chl_{2A}/Chl_{3A} and Chl_{3A}/Chl_{3B} act as dimers in which the spin density is delocalized over both chlorophyll molecules.[37] In HbRCs the corresponding chlorophylls BChl *g* and Chl a_F have a very similar structural arrangement to $Chl_{2A/B}$ and $Chl_{3A/B}$ in Photosystem I. Thus, it is likely that the spin density is also distributed over both chlorophylls in HbRCs and conversion of BChl *g* to Chl a_F would likely result in a change in the spin density distribution in A_0^-. If such a change could be observed in dioxygen exposed samples, it would provide further evidence that conversion of the accessory BChl *g* does not prevent charge separation. This would also support the hypothesis that the initial charge separation is between P_{800} and the accessory chlorophyll in oxygen exposed RCs because electron transfer between the Chl a_F in the accessory chlorophyll site and Chl a_F in the A_0 site is probably not energetically viable. We are currently carrying out quantum chemical calculations of acceptor chlorophylls in HbRCs to test this idea.

.

Conflicts of interest

There are no conflicts to declare.

Acknowledgements

This work was supported by a Discovery Grant from the Natural Science and Engineering Research Council of Canada to AvdE (Discovery Grant No. 2015-04021) and by the Photosynthetic Systems Program, Office of Basic Energy Sciences of the U. S. Department of Energy under the contracts DE-FG02-07ER15903 (KVL) and DE-SC0010575 (JHG). PL acknowledges support from the National Science Foundation Graduate Research Fellowship Program (NSF GRFP) and DK acknowledges start-up funding support from Brock University. SW thanks the SIBW/DFG for financing EPR instrumentation that is operated within the MagRes Center of the Albert-Ludwigs-Universität Freiburg (Germany). This work was made possible by the facilities of the Shared Hierarchical Academic Research Computing Network (SHARCNET:www.sharcnet.ca) and Compute/Calcul Canada.

Notes and references

1 H. Gest and J. L. Favinger, *Heliobacterium chlorum*, an anoxygenic brownish-green photosynthetic bacterium containing a "new" form of bacteriochlorophyll, *Arch. Microbiol.*, 1983, **136**, 11–16.

2 C. Gisriel, I. Sarrou, B. Ferlez, J. H. Golbeck, K. E. Redding and R. Fromme, Structure of a symmetric photosynthetic reaction center–photosystem, *Science*, 2017, **357**, 1021–1025.

3 B. Ferlez, W. Dong, R. Siavashi, K. Redding, H. J. Hou, J. H. Golbeck and A. van der Est, The effect of bacteriochlorophyll *g* oxidation on energy and electron transfer in reaction centers from *Heliobacterium modesticaldum*, *J. Phys. Chem. B*, 2015, **119**, 13714–13725.

4 M. Kobayashi, T. Hamano, M. Akiyama, T. Watanabe, K. Inoue, H. Oh-oka, J. Amesz, M. Yamamura and H. Kise, Light-independent isomerization of bacteriochlorophyll *g* to chlorophyll *a* catalyzed by weak acid in vitro, *Anal. Chim. Acta*, 1998, **365**, 199–203.

5 P. Beer-Romero, J. L. Favinger and H. Gest, Distinctive properties of bacilliform photosynthetic heliobacteria, *FEMS Microbiol. Lett.*, 1988, **49**, 451–454.

6 S. Surendran Thamarath, A. Alia, E. Roy, K. B. Sai Sankar Gupta, J. H. Golbeck and J. Matysik, The field-dependence of the solid-state photo-CIDNP effect in two states of heliobacterial reaction centers, *Photosynth. Res.*, 2013, **117**, 461–469.

7 G. P. Moss, Nomenclature of tetrapyrroles: recommendations 1986, *Eur. J. Biochem.*, 1988, **178**, 277–328.

8 M. Heinnickel, R. Agalarov, N. Svensen, C. Krebs and J. H. Golbeck, Identification of F_X in the heliobacterial reaction center as a [4Fe-4S] cluster with an S= 3/2 ground spin state, *Biochemistry*, 2006, **45**, 6756–6764.

9 S. Stoll and A. Schweiger, EasySpin, a comprehensive software package for spectral simulation and analysis in EPR, *J. Magn. Reson.*, 2006, **178**, 42–55.

10 S. Stoll and R. D. Britt, General and efficient simulation of pulse EPR spectra, *Phys. Chem. Chem. Phys.*, 2009, **11**, 6614–6625.
11 A. Schweiger and G. Jeschke, *Principles of Pulse Paramagnetic Resonance*, Oxford university press, Oxford, 2001.
12 P. Höfer, A. Grupp, H. Nebenführ and M. Mehring, Hyperfine sublevel correlation (HYSCORE) spectroscopy: a 2D ESR investigation of the squaric acid radical, *Chem. Phys. Lett.*, 1986, **132**, 279–282.
13 C. S. Coates, S. Milikisiyants, R. Chatterjee, M. M. Whittaker, J. W. Whittaker and K. V. Lakshmi, Two-dimensional HYSCORE spectroscopy of superoxidized manganese catalase: a model for the oxygen-evolving complex of photosystem II, *J. Phys. Chem. B*, 2015, **119**, 4905–4916.
14 S. Milikisiyants, R. Chatterjee, A. Weyers, A. Meenaghan, C. Coates and K. V. Lakshmi, Ligand environment of the S2 state of photosystem II: a study of the hyperfine interactions of the tetranuclear manganese cluster by 2D 14N HYSCORE spectroscopy, *J. Phys. Chem. B*, 2010, **114**, 10905–10911.
15 F. Neese, F. Wennmohs, U. Becker and C. Riplinger, The ORCA quantum chemistry program package, *J. Chem. Phys.*, 2020, **152**, 224108.
16 J. G. Brandenburg, C. Bannwarth, A. Hansen and S. Grimme, B97-3c: A revised low-cost variant of the B97-D density functional method, *J. Chem. Phys.*, 2018, **148**, 064104.
17 J. P. Perdew, K. Burke and M. Ernzerhof, Generalized gradient approximation made simple, *Phys. Rev. Lett.*, 1996, **77**, 3865.
18 W. J. Hehre, R. Ditchfield and J. A. Pople, Self—Consistent Molecular Orbital Methods. XII. Further Extensions of Gaussian—Type Basis Sets for Use in Molecular Orbital Studies of Organic Molecules, *J. Chem. Phys.*, 1972, **56**, 2257–2261.
19 M. M. Francl, W. J. Pietro, W. J. Hehre, J. S. Binkley, M. S. Gordon, D. J. DeFrees and J. A. Pople, Self-consistent molecular orbital methods. XXIII. A polarization-type basis set for second-row elements, *J. Chem. Phys.*, 1982, **77**, 3654–3665.
20 S. Grimme, S. Ehrlich and L. Goerigk, Effect of the damping function in dispersion corrected density functional theory, *J. Comput. Chem.*, 2011, **32**, 1456–1465.
21 S. Grimme, J. Antony, S. Ehrlich and H. Krieg, A consistent and accurate ab initio parametrization of density functional dispersion correction (DFT-D) for the 94 elements H-Pu, *J. Chem. Phys.*, 2010, **132**, 154104.
22 R. A. Kendall and H. A. Früchtl, The impact of the resolution of the identity approximate integral method on modern ab initio algorithm development, *Theor. Chem. Acc.*, 1997, **97**, 158–163.
23 M. Sierka, A. Hogekamp and R. Ahlrichs, Fast evaluation of the Coulomb potential for electron densities using multipole accelerated resolution of identity approximation, *J. Chem. Phys.*, 2003, **118**, 9136–9148.
24 K. Eichkorn, O. Treutler, H. Öhm, M. Häser and R. Ahlrichs, Auxiliary basis sets to approximate Coulomb potentials, *Chem. Phys. Lett.*, 1995, **240**, 283–290.
25 M. D. Hanwell, D. E. Curtis, D. C. Lonie, T. Vandermeersch, E. Zurek and G. R. Hutchison, Avogadro: an advanced semantic chemical editor, visualization, and analysis platform, *J. Cheminformatics*, 2012, **4**, 17.
26 J.-D. Chai and M. Head-Gordon, Long-range corrected hybrid density functionals with damped atom–atom dispersion corrections, *Phys. Chem. Chem. Phys.*, 2008, **10**, 6615–6620.
27 F. Weigend and R. Ahlrichs, Balanced basis sets of split valence, triple zeta valence and quadruple zeta valence quality for H to Rn: Design and assessment of accuracy, *Phys. Chem. Chem. Phys.*, 2005, **7**, 3297–3305.
28 F. Neese, F. Wennmohs, A. Hansen and U. Becker, Efficient, approximate and parallel Hartree–Fock and hybrid DFT calculations. A 'chain-of-spheres' algorithm for the Hartree–Fock exchange, *Chem. Phys.*, 2009, **356**, 98–109.
29 K. Eichkorn, O. Treutler, H. Öhm, M. Häser and R. Ahlrichs, Auxiliary basis sets to approximate Coulomb potentials, *Chem. Phys. Lett.*, 1995, **240**, 283–290.
30 F. Weigend, Accurate Coulomb-fitting basis sets for H to Rn, *Phys. Chem. Chem. Phys.*, 2006, **8**, 1057–1065.
31 J. R. Norris, R. A. Uphaus, H. L. Crespi and J. J. Katz, Electron spin resonance of chlorophyll and the origin of signal I in photosynthesis, *Proc. Natl. Acad. Sci.*, 1971, **68**, 625–628.
32 S. E. Rigby, M. C. Evans and P. Heathcote, Electron nuclear double resonance (ENDOR) spectroscopy of radicals in photosystem I and related Type 1 photosynthetic reaction centres, *Biochim. Biophys. Acta*, 2001, **1507**, 247–259.
33 J. Rautter, B. Bönigk and W. Lubitz, ENDOR Studies of the Cation Radical of the Primary Donor in Heliobacteria Suggest that P798+ is a Symmetric Dimer, *Biophys. J.*, 1996, **70**, A141.
34 I. García-Rubio, J. I. Martínez, R. Picorel, I. Yruela and P. J. Alonso, HYSCORE spectroscopy in the cytochrome b(559) of the photosystem II reaction center, *J. Am. Chem. Soc.*, 2003, **125**, 15846–15854.
35 Y. Deligiannakis, M. Louloudi and N. Hadjiliadis, Electron spin echo envelope modulation (ESEEM) spectroscopy as a tool to investigate the coordination environment of metal centers, *Coord. Chem. Rev.*, 2000, **204**, 1–112.
36 S. Van Doorslaer, Understanding heme proteins with hyperfine spectroscopy, *J. Magn. Reson. San Diego Calif 1997*, 2017, **280**, 79–88.
37 M. Gorka, P. Charles, V. Kalendra, A. Baldansuren, K. V. Lakshmi and J. H. Golbeck, A dimeric chlorophyll electron acceptor differentiates type I from type II photosynthetic reaction centers, *iScience*, 2021, **24**, 102719.
38 P. Charles, V. Kalendra, Z. He, M. H. Khatami, J. H. Golbeck, A. van der Est, K. V. Lakshmi and D. A. Bryant, Two-dimensional ^{67}Zn HYSCORE spectroscopy reveals that a Zn-bacteriochlorophyll $a_{P'}$ dimer is the primary donor (P_{840}) in the type-1 reaction centers of *Chloracidobacterium thermophilum*, *Phys. Chem. Chem. Phys.*, 2020, **22**, 6457–6467.
39 M. J. Gorka, A. Baldansuren, A. Malnati, E. Gruszecki, J. H. Golbeck and K. V. Lakshmi, Shedding light on primary donors in photosynthetic reaction centers, *Front. Microbiol.*, 2021, **12**, 735666.
40 P. J. Bratt, I. P. Muhiuddin, M. C. Evans and P. Heathcote, 14N electron spin echo envelope modulation (ESEEM) spectroscopy of the cation radical P_{840}^+, the primary electron donor of the *Chlorobium limicola* reaction center, *Photochem. Photobiol.*, 1996, **64**, 20–25.
41 M. M. Chestnut, S. Milikisiyants, R. Chatterjee, J. Kern and A. I. Smirnov, Electronic structure of the primary electron donor $P_{700}^{+\bullet}$ in photosystem I studied by multifrequency HYSCORE spectroscopy at X-and Q-band, *J. Phys. Chem. B*, 2020, **125**, 36–48.
42 H. Käss, J. Rautter, B. Bönigk, P. Höfer and W. Lubitz, 2D ESEEM of the 15N-Labeled Radical Cations of Bacteriochlorophyll *a* and of the Primary Donor in Reaction Centers of *Rhodobacter sphaeroides*, *J. Phys. Chem.*, 1995, **99**, 436–448.
43 H. Käβ, P. Fromme and W. Lubitz, Quadrupole parameters of nitrogen nuclei in the cation radical $P_{700}^{\cdot+}$ determined by ESEEM of single crystals of phtosystem I, *Chem. Phys. Lett.*, 1996, **257**, 197–206.

44 M. Plato, N. Krauß, P. Fromme and W. Lubitz, Molecular orbital study of the primary electron donor P_{700} of photosystem I based on a recent X-ray single crystal structure analysis, *Chem. Phys.*, 2003, **294**, 483–499.
45 A. N. Webber and W. Lubitz, P700: the primary electron donor of photosystem I, *Biochim. Biophys. Acta*, 2001, **1507**, 61–79.
46 M. Brütting, J. M. Foerster and S. Kümmel, Investigating primary charge separation in the reaction center of *heliobacterium modesticaldum*, *J. Phys. Chem. B*, 2021, **125**, 3468–3475.
47 M. Brütting, J. M. Foerster and S. Kümmel, Understanding Primary Charge Separation in the Heliobacterial Reaction Center, *J. Phys. Chem. Lett.*, 2023, **14**, 3092–3102.
48 G. S. Orf and K. E. Redding, Perturbation of the primary acceptor chlorophyll site in the heliobacterial reaction center by coordinating amino acid substitution, *Biochim. Biophys. Acta BBA-Bioenerg.*, 2021, **1862**, 148324.
49 Y. Song, R. Sechrist, H. H. Nguyen, W. Johnson, D. Abramavicius, K. E. Redding and J. P. Ogilvie, Excitonic structure and charge separation in the heliobacterial reaction center probed by multispectral multidimensional spectroscopy, *Nat. Commun.*, 2021, **12**, 2801.
50 M. Gorka, P. Landry, E. Gruszecki, A. Malnati, D. Kaur, A. van der Est, J. H. Golbeck and K. V. Lakshmi, in *Photosynthesis*, eds. H. J. M. Hou and S. I. Allakhverdiev, Academic Press, 2023, pp. 197–237.